Two Decades of Wave-Like Equation for the Numerical Simulation of Incompressible Viscous Flow: A Review

Roland Glowinski and Tsorng-Whay Pan

Abstract A wave-like equation based method for the numerical solution of the Navier-Stokes equations modeling incompressible viscous flow was introduced nearly twenty years ago. From its inception to nowadays it has been applied successfully to the numerical solution of two and three dimensional flow problems for incompressible Newtonian and non-Newtonian viscous fluids, in flow regions with fixed or moving boundaries. The main goals of this article are: (i) To recall the foundations of the wave-like equation methodology, and (ii) to review some typical viscous flow problems where it has been applied successfully.

Keywords Incompressible viscous flow · Operator splitting time discretization schemes · Wave-like equation method for the numerical treatment of the advection step · Finite element approximations

1 Introduction

Some time ago, the authors of this article were asked to contribute to a volume dedicated to their colleagues and friends *W. Fitzgibbon*, *Y. Kuznetsov* and *O. Pironneau* on the occasion of their 70th anniversary. The authors decided to take advantage of this special volume to celebrate another anniversary: Indeed, nearly twenty years ago, they dropped the nonlinear least-squares methodology they have been using for years for the numerical treatment of the advection operator, encountered in the

Dedicated to W. Fitzgibbon, Y. Kuznetsov and O. Pironneau on the occasion of their 70th anniversary.

R. Glowinski (✉) · T.-W. Pan
Department of Mathematics, University of Houston, Houston, TX 77204, USA
e-mail: roland@math.uh.edu

T.-W. Pan
e-mail: pan@math.uh.edu

R. Glowinski
Department of Mathematics, Hong-Kong Baptist University, Kowloon Tong, Hong Kong

B. N. Chetverushkin et al. (eds.), *Contributions to Partial Differential Equations and Applications*, Computational Methods in Applied Sciences 47,
https://doi.org/10.1007/978-3-319-78325-3_13

Navier-Stokes equations modelling *incompressible viscous flow*, and started employing systematically a novel methodology based on a *wave-like equation* modelling of the advection. From then to now, the wave-like equation method has been successfully applied, by the authors and other people, to the numerical simulation of a rather large variety of incompressible viscous flows, justifying in the authors opinion a relatively detailed dedicated review publication. The content of this article is as follows: In Sect. 2, we will describe the wave-like equation method when applied to the numerical solution of the Navier-Stokes equations modelling incompressible viscous flow, and take advantage of this section to provide related references. In Sects. 3–5 we will describe and comment on several successful applications of the wave-like equation based methodology; they concern Newtonian, visco-elastic and particulate viscous flows.

2 The Wave-Like Equation Method for the Incompressible Navier-Stokes Equations

Our starting point will be the *Navier-Stokes equations* modeling the flow of *incompressible Newtonian viscous fluids*, namely

$$\begin{cases} \rho\left[\dfrac{\partial \mathbf{u}}{\partial t} + (\mathbf{u}\cdot\nabla)\mathbf{u}\right] - \mu\nabla^2\mathbf{u} + \nabla p = \mathbf{f} \quad \text{in } \Omega\times(0,T), \\ \nabla\cdot\mathbf{u} = 0 \quad \text{in } \Omega\times(0,T), \\ \mathbf{u}(0) = \mathbf{u}_0 \quad \text{with} \quad \nabla\cdot\mathbf{u}_0 = 0, \\ \mathbf{u} = \mathbf{u}_B \quad \text{on } \Gamma\times(0,T) \quad \text{with} \quad \displaystyle\int_\Gamma \mathbf{u}_B(t)\cdot\mathbf{n}\,d\Gamma = 0 \quad \text{on } (0,T), \end{cases} \tag{1}$$

where:

- Ω (a sub-domain of $\mathbb{R}^d$, $d = 2$ or 3) is the flow region, and $0 < T \leq +\infty$. We denote by Γ the boundary of Ω.
- $\mathbf{u}$ (resp., p) denotes the flow velocity (resp., pressure), and $\mathbf{f}$ a density of external forces.
- ρ and μ are both > 0, and denote the fluid density and viscosity, respectively.
- $\phi(t)$ denotes the function $\mathbf{x} \to \phi(\mathbf{x}, t)$ (with $\mathbf{x} = \{x_i\}_{i=1}^d$).
- $\mathbf{n}$ denotes the unit outward normal vector at Γ.

The numerical solution of problem (1) has generated a most abundant literature (see, in particular, the related references provided by *Google Scholar*). Among the many methods for the numerical solution of (1), we will single out those based on *operator-splitting*. Applying the *Lie scheme* (see, e.g., [20, 21, 25] for a general discussion of that scheme), we obtain (among other possibilities) the following time-discretization of problem (1) (with $\triangle t(>0)$ a time-discretization step and $t^n = n\triangle t$):

$$\mathbf{u}^0 = \mathbf{u}_0. \tag{2}$$

For $n \geq 0, \mathbf{u}^n \rightarrow \{\mathbf{u}^{n+1/2}, p^{n+1}\} \rightarrow \mathbf{u}^{n+1}$ *via the solution of*

$$\begin{cases} \rho \dfrac{\mathbf{u}^{n+1/2} - \mathbf{u}^n}{\triangle t} - \mu \nabla^2 \mathbf{u}^{n+1/2} + \nabla p^{n+1} = \mathbf{f}^{n+1} & \text{in } \Omega, \\ \nabla \cdot \mathbf{u}^{n+1/2} = 0 & \text{in } \Omega, \\ \mathbf{u}^{n+1/2} = \mathbf{u}_B(t^{n+1}) & \text{on } \Gamma, \end{cases} \tag{3}$$

and

$$\begin{cases} \dfrac{\partial \mathbf{w}}{\partial t} + (\mathbf{u}^{n+1/2} \cdot \nabla)\mathbf{w} = \mathbf{0} & \text{in } \Omega \times (t^n, t^{n+1}), \\ \mathbf{w}(t^n) = \mathbf{u}^{n+1/2}, & \\ \mathbf{w}(t) = \mathbf{u}^{n+1/2} (= \mathbf{u}_B(t^{n+1})) & \text{on } \Gamma_-^{n+1} \times (t^n, t^{n+1}), \end{cases} \tag{4.1}$$

$$\mathbf{u}^{n+1} = \mathbf{w}(t^{n+1}), \tag{4.2}$$

with $\Gamma_-^{n+1} = \{\mathbf{x} \mid \mathbf{x} \in \Gamma, \mathbf{u}_B(\mathbf{x}, t^{n+1}) \cdot \mathbf{n}(\mathbf{x}) < 0\}$.

Remark 1 The time discretization of problem (1) by the *Strang symmetrized scheme* (a more sophisticated variant of the Lie scheme) is discussed in [12, 20] (see also the references therein). □

The solution of the (generalized) Stokes problem (3) being a well-documented (and different) issue (see, e.g., [3, 20]), we will focus on the most controversial part of scheme (2)–(4), namely the solution of the initial value problem (4.1). One can easily show that in (4.1), each component of $\mathbf{w}$ is solution of an initial-boundary value problem of the following type:

$$\begin{cases} \dfrac{\partial \phi}{\partial t} + \mathbf{V} \cdot \nabla \phi = 0 & \text{in } \Omega \times (t_0, t_f), \\ \phi(t_0) = \phi_0, & \\ \phi = g & \text{on } \Gamma_- \times (t_0, t_f), \end{cases} \tag{5}$$

where $\frac{\partial \mathbf{V}}{\partial t} = \mathbf{0}, \nabla \cdot \mathbf{V} = 0, \frac{\partial g}{\partial t} = 0$, and $\Gamma_- = \{\mathbf{x} \mid \mathbf{x} \in \Gamma, \mathbf{V}(\mathbf{x}) \cdot \mathbf{n}(\mathbf{x}) < 0\}$.

The solution of first order problems such as (5) has motivated a very large literature (see, e.g., [28] and the references therein). It seems thus that one has abundance of methods to solve the problem (5); this is definitely true, but things get complicated if one wishes to solve problem (4.1) using the same finite element velocity spaces that one employs for the solution of the problem (3). A conceptually elegant way to achieve that goal is to use the *backward method of characteristics* as done in, e.g., [52, 57, 58] via the so-called *Lagrange-Galerkin* methodology. Albeit conceptually simple the practical implementation of the Lagrange-Galerkin methods requires a lot of 'savoir faire' (see [58] for an evidence of the above statement). Fortunately, there exists a very simple alternative to the method of characteristics, based on a wave-like equation reformulation of the problem (5). We personally encountered this approach when investigating the wavelet solution (see [24]) of

$$\begin{cases} \dfrac{\partial u}{\partial t} + a\dfrac{\partial u}{\partial x} = 0 \quad \text{in } (0, L) \times (0, T), \\ u(0) = u_0, \\ u(0, t) = g(t), \quad t \in (0, T), \end{cases} \tag{6}$$

with: $0 < L < +\infty$, a a positive number, and $0 < T \leq +\infty$. If the functions u_0 and g are smooth enough, one can easily show (by time differentiation of the first equation in (6); see [12, 20] for details) that problem (6) has a unique solution which is also the unique solution of the following (genuine) wave equation problem:

$$\begin{cases} \dfrac{\partial^2 u}{\partial t^2} - a^2\dfrac{\partial^2 u}{\partial x^2} = 0 \quad \text{in } (0, L) \times (0, T), \\ u(0) = u_0, \quad \dfrac{\partial u}{\partial t}(0) = -a\dfrac{\partial u_0}{\partial x}, \\ u(0, t) = g(t), \quad \dfrac{\partial u}{\partial t}(L, t) + a\dfrac{\partial u}{\partial x}(L, t) = 0, \quad t \in (0, T); \end{cases} \tag{7}$$

the boundary condition at $x = L$ can be viewed as a *radiation condition*. Assuming that u is smooth enough, problem (7) has the following variational formulation:

$$\begin{cases} u(t) \in H^1(0, L), \quad u(0, t) = g(t), \quad t \in (0, T), \\ \displaystyle\int_0^L \frac{\partial^2 u}{\partial t^2} v\, dx + a^2 \int_0^L \frac{\partial u}{\partial x}(t)\frac{\partial v}{\partial x}\, dx + a\frac{\partial u}{\partial t}(L, t)v(L) = 0, \\ \forall v \in V_0,\ t \in (0, T), \\ u(0) = u_0, \quad \dfrac{\partial u}{\partial t}(0) = -a\dfrac{\partial u_0}{\partial x}, \end{cases} \tag{8}$$

with $V_0 = \{v \mid v \in H^1(0, L),\ v(0) = 0\}$. Thanks to variational formulation (8), problem (7), and therefore problem (6), can be solved by *finite element methods* of the Lagrange-Galerkin type (including those based on the Courant element, that is piecewise affine, globally continuous approximations) or (as done in [24]) by wavelet-Galerkin methods.

Remark 2 The approach we just advocated for the solution contradicts the popular approach which consists in writing second order in time differential equations as systems of first order ones. □

Actually, the strategy we just described for problem (6) can be easily generalized to problem (5) by observing that the properties $\nabla \cdot \mathbf{V} = 0$ and $\frac{\partial \mathbf{V}}{\partial t} = \mathbf{0}$ imply that, after time differentiation, any smooth solution of problem (5) is solution of

$$\begin{cases} \dfrac{\partial^2 \phi}{\partial t^2} - \nabla \cdot ((\mathbf{V} \cdot \nabla\phi)\mathbf{V}) = 0, \quad \text{in } \Omega \times (t_0, t_f), \\ \phi(t_0) = \phi_0, \quad \dfrac{\partial \phi}{\partial t}(t_0) = -\mathbf{V} \cdot \nabla\phi_0, \\ \phi = g \quad \text{on } \Gamma_- \times (t_0, t_f), \quad (\mathbf{V} \cdot \mathbf{n})\left(\dfrac{\partial \phi}{\partial t} + \mathbf{V} \cdot \nabla\phi\right) = 0 \quad \text{on } \Gamma \setminus \Gamma_- \times (t_0, t_f), \end{cases} \tag{9}$$

a wave-like equation problem associated with the *hypo-elliptic* operator

$$\phi \to -\nabla \cdot ((\mathbf{V} \cdot \nabla \phi)\mathbf{V}).$$

Let us define the space V_0 by

$$V_0 = \{\theta \mid \theta \in H^1(\Omega), \quad \theta = 0 \text{ on } \Gamma_-\};$$

assuming that problem (9) has a smooth enough solution, using the *divergence theorem*, one can easily show that the above problem has the following *variational formulation* (with $d\mathbf{x} = dx_1 \dots dx_d$):

$$\begin{cases} \phi(t) \in H^1(\Omega), \quad \phi(t)|_{\Gamma_-} = g, \quad t \in (t_0, t_f), \\ \displaystyle\int_\Omega \frac{\partial^2 \phi}{\partial t^2}\theta \, d\mathbf{x} + \int_\Omega (\mathbf{V} \cdot \nabla \phi)(\mathbf{V} \cdot \nabla \theta) \, d\mathbf{x} + \int_{\Gamma \setminus \Gamma_-} \mathbf{V} \cdot \mathbf{n} \frac{\partial \phi}{\partial t}\theta \, d\Gamma = 0, \\ \forall \theta \in V_0, \quad t \in (t_0, t_f), \\ \phi(t_0) = \phi_0, \quad \dfrac{\partial \phi}{\partial t}(t_0) = -\mathbf{V} \cdot \nabla \phi_0. \end{cases} \tag{10}$$

From (10), one can easily show that if problem (9) has a solution, it is unique. Formulation (10) is ideally suited to *Lagrange finite element approximations* as shown in, e.g., [12, 20], where it has been (successfully) applied in combination with the finite element spaces used for the numerical solution of the Stokes-like problem (3). Concerning the *time-discretization* of (10), we have been advocating the following *centered scheme* (with $\tau = \frac{t_f - t_0}{Q}$, the integer Q being >1):

$$\phi^0 = \phi_0, \quad \phi^1 - \phi^{-1} = 2\tau \phi_1. \tag{11}$$

For $q = 0, 1, \dots, Q-1$, $\{\phi^{q-1}, \phi^q\} \to \phi^{q+1}$ as follows:

$$\begin{cases} \phi^{q+1} \in H^1(\Omega), \quad \phi^{q+1}|_{\Gamma_-} = g, \\ \displaystyle\int_\Omega \frac{\phi^{q+1} + \phi^{q-1} - 2\phi^q}{\tau^2}\theta \, d\mathbf{x} + \int_\Omega (\mathbf{V} \cdot \nabla \phi^q)(\mathbf{V} \cdot \nabla \theta) \, d\mathbf{x} \\ \quad + \displaystyle\int_{\Gamma \setminus \Gamma_-} \mathbf{V} \cdot \mathbf{n} \left(\frac{\phi^{q+1} - \phi^{q-1}}{2\tau} \right) \theta \, d\Gamma = 0, \quad \forall \theta \in V_0, \end{cases} \tag{12}$$

where, in (11), ϕ_1 is solution of the following variational problem:

$$\begin{cases} \phi_1 \in V_0, \\ \displaystyle\int_\Omega \phi_1 \theta \, d\mathbf{x} = -\int_\Omega \mathbf{V} \cdot \nabla \phi_0 \theta \, d\mathbf{x}, \quad \forall \theta \in V_0. \end{cases} \tag{13}$$

Strictly speaking, the infinite dimensional variational problems (12) and (13) make no sense, in general, unlike, fortunately, their finite dimensional analogues, obtained from (12) and (13) via appropriate finite element approximations (see [12, 20] for details).

Remark 3 As expected, the wave-like equation method described above is not a *stand-alone* one for the numerical solution of advection problems such (5), as shown by the numerical experiments reported in [20]. The reason for that unfortunate situation is easy to understand: the wave-like equation in (9) is a model for propagation in both the $\mathbf{V}$ and $-\mathbf{V}$ directions; with appropriate initial and boundary conditions, there is no 'signal' propagating in the $-\mathbf{V}$ direction. However these ideal circumstances do not hold *exactly* anymore after space-time discretization, explaining the existence of a small (if $\triangle x$ and $\triangle t$ are small) parasitic signal propagating in the $-\mathbf{V}$ direction. The good news are that when using the wave-like equation method to solve the incompressible Navier-Stokes equations, the advection step (4) is combined with the incompressible-viscous step (3), the solver of the problem (3) filtering (at least partially) those unwanted oscillations generated by the solver of the problem (9), (10).

Remark 4 When applying the wave-like equation method to solve the incompressible Navier equations via the Lie-scheme (2)–(4), we advocate taking $\tau = \triangle t/Q$, with $2 \leq Q \leq 5$, in the fully discrete analogue of scheme (11), (12).

Remark 5 To the best of our knowledge, the wave-like equation method for the solution of the incompressible Navier-Stokes equations has been introduced in [10]. Actually, a related method was introduced in 1979 by *Lynch and Gray* for the solution of the *shallow water equations* [44], the convergence of the method being discussed in [7, 8]. See also [60, 61] for the application of a closely related method to the solution of *multi-dimensional transport problems*. □

Since its introduction in 1997 the wave-like equation/operator-splitting method discussed above has been applied by the authors, their students, post-docs and other collaborators and scientists to a large variety of viscous-flow problems, some more complicated than problem (1). Let us mention among others: (i) The numerical simulation of *particulate flow* (see, e.g., [20, 26, 31]). (ii) The numerical solution of the *Boussinesq system* coupling the *Navier-Stokes* and *heat equations*, and modelling *natural convection* [20]. (iii) The simulation of *visco-plastic flow* [11, 20, 27]. (iv) The simulation of *visco-elastic flow* (possibly with particles) [20, 48, 49]. (v) The solution of *free boundary problems* for incompressible viscous flow [22]. (vi) The numerical solution of the system coupling the *Cahn-Hilliard* and *Navier-Stokes equations* and modelling the flow of multiple immiscible incompressible viscous fluids [30]. The references in the above publications are also worth consulting.

Other examples and further references will be given in Sects. 3–5.

To conclude this introductory section we cannot resist mentioning the fact that some of the results from [23], concerning operator-splitting/wave-like equation based simulations of wall-driven incompressible viscous flows in a *semi-circular cavity*, have been used in [59] to validate a *NURBS* (for *Non Uniform Rational Bézier Splines*) based Navier-Stokes solver.

3 On the Simulation of 3-D Incompressible Viscous Flow in a Cube with a Moving Wall

3.1 Generalities

Starting with [18], the wall-driven square cavity flow problem has been for decades the most popular problem used to validate and compare incompressible Navier-Stokes solvers. No surprisingly, it has been used by the two authors and their collaborators to validate the operator-splitting/wave like equation method briefly discussed in Sect. 1, some of the results of the related simulations being reported in [12, 20]. Actually, one has also reported in ([20], Chap. 9) and [47] the results of the simulation of a Newtonian incompressible viscous flow in a cubic cavity when one of the walls is sliding; the maximal Reynolds number (Re) considered in [20, 47] is 10^3. More recently the oscillatory instability of cubic lid-driven cavity flows has been studied in [1, 16, 41]. Numerically, Feldman and Gelfgat [16] obtained that the critical Reynolds number for the transition from a steady flow to an oscillatory one (a Hopf bifurcation) is at $\mathrm{Re}_{cr} = 1914$. Anupindi et al. [1] reported that the critical Re they observed is $\mathrm{Re}_{cr} = 2300$, which was obtained using regularized boundary condition. Experimentally, Liberzon et al. [41] reported that the critical Reynolds number is in the range [1700, 1970], One of our goals in this section is to report on the results we obtained when taking Re beyond 10^3, and to identify as accurately as possible the value of Re at which a Hopf bifurcation does occur.

3.2 Numerical Methods

To speed up the numerical solution of the cubic lid-driven cavity flow problem, we time-discretized the related problem (1), using a three stage operator-splitting scheme, namely: (i) using a L^2-projection Stokes solver à la Uzawa to force the incompressibility condition, (ii) an advection step similar to (4), and (iii) a diffusion step. The resulting scheme reads as follows:

$$\mathbf{u}^0 = \mathbf{u}_0. \tag{14}$$

For $n \geq 0, \mathbf{u}^n \rightarrow \{\mathbf{u}^{n+1/3}, p^{n+1}\} \rightarrow \mathbf{u}^{n+2/3} \rightarrow \mathbf{u}^{n+1}$ via the solution of:

$$\begin{cases} \rho \dfrac{\mathbf{u}^{n+1/3} - \mathbf{u}^n}{\triangle t} + \nabla p^{n+1} = \mathbf{0} & \text{in } \Omega, \\ \nabla \cdot \mathbf{u}^{n+1/3} = 0 & \text{in } \Omega, \\ \mathbf{u}^{n+1/3} \cdot \mathbf{n} = 0 & \text{on } \Gamma, \end{cases} \tag{15}$$

$$\begin{cases} \dfrac{\partial \mathbf{w}}{\partial t} + (\mathbf{u}^{n+1/3} \cdot \nabla)\mathbf{w} = \mathbf{0} & \text{in } \Omega \times (t^n, t^{n+1}), \\ \mathbf{w}(t^n) = \mathbf{u}^{n+1/3}, \\ \mathbf{w}(t) = \mathbf{u}^{n+1/3} (= \mathbf{u}_B(t^{n+1})) & \text{on } \Gamma_-^{n+1} \times (t^n, t^{n+1}), \end{cases} \tag{16.1}$$

$$\mathbf{u}^{n+2/3} = \mathbf{w}(t^{n+1}), \tag{16.2}$$

$$\begin{cases} \rho \dfrac{\mathbf{u}^{n+1} - \mathbf{u}^{n+2/3}}{\triangle t} - \mu \nabla^2 \mathbf{u}^{n+1} = \mathbf{f}^{n+1} & \text{in } \Omega, \\ \mathbf{u}^{n+1} = \mathbf{u}_B(t^{n+1}) & \text{on } \Gamma. \end{cases} \tag{17}$$

Two simplifications take place for the lid-driven cavity flow problem considered here: namely, $\mathbf{f}^{n+1} = \mathbf{0}$ and $\Gamma_-^{n+1} = \emptyset$. For the space discretization, we have used, as in ([20], Chap. 5) and [3], a P_1-*iso*-P_2 (resp., P_1) finite element method for the approximation of the velocity field (resp., pressure), defined from uniform "tetrahedral" meshes $\mathcal{T}_h$ (resp., $\mathcal{T}_{2h}$). Problem (15) is reminiscent of those encountered when applying Chorin's projection method [9].

3.3 Numerical Results

For the lid-driven cavity flow problem in a cube, considered here, we took $\Omega = (0, 1)^3$ as computational domain and defined the Dirichlet data $\mathbf{u}_B$ by

$$\mathbf{u}_B(\mathbf{x}) = \begin{cases} (1, 0, 0)^T & \text{on } \{\mathbf{x} \mid \mathbf{x} = (x_1, x_2, 1)^T,\ 0 < x_1,\ x_2 < 1\}, \\ \mathbf{0} & \text{elsewhere on } \Gamma. \end{cases} \tag{18}$$

We considered that the steady state has been reached when the change between two consecutive time step in the simulation, $\|\mathbf{u}_h^n - \mathbf{u}_h^{n-1}\|_\infty / \triangle t$, is less than 10^{-4}, and then took $\mathbf{u}_h^n$ as the steady state solution.

To validate the numerical methodology, we have considered for the velocity mesh size the values $h = 1/60$ and $1/96$ associated with the time step $\triangle t = 0.001$. For $\mathrm{Re} = 400$ and 1000, the results reported in Fig. 1 show a very good agreement with those obtained in [5, 17, 39]. The velocity vectors of the steady flows obtained for $\mathrm{Re} = 400$ and 1000 are shown in Fig. 2. Those velocity field vectors are projected orthogonally to the three planes, $x_2 = 0.5$, $x_1 = 0.5$, and $x_3 = 0.5$, and the length of the vectors has been doubled in the two later planes to observe the flow more clearly.

To study the transition from steady flow to oscillatory flow, we have analyzed the history of the L^2-norm $\|\mathbf{u}_h^n\|$ of the flow field for different values of Re and of the mesh size h. For $h = 1/60$, the flow field evolves to a steady state for $\mathrm{Re} \leq 1860$ and the amplitude of the oscillation of the flow field L^2-norm decreases also in time. At $\mathrm{Re} = 1865$, the steady state criterion is not satisfied and the amplitude of the oscillation increases in time as in Fig. 3. Thus we conclude that the critical Reynolds number Re_{cr}

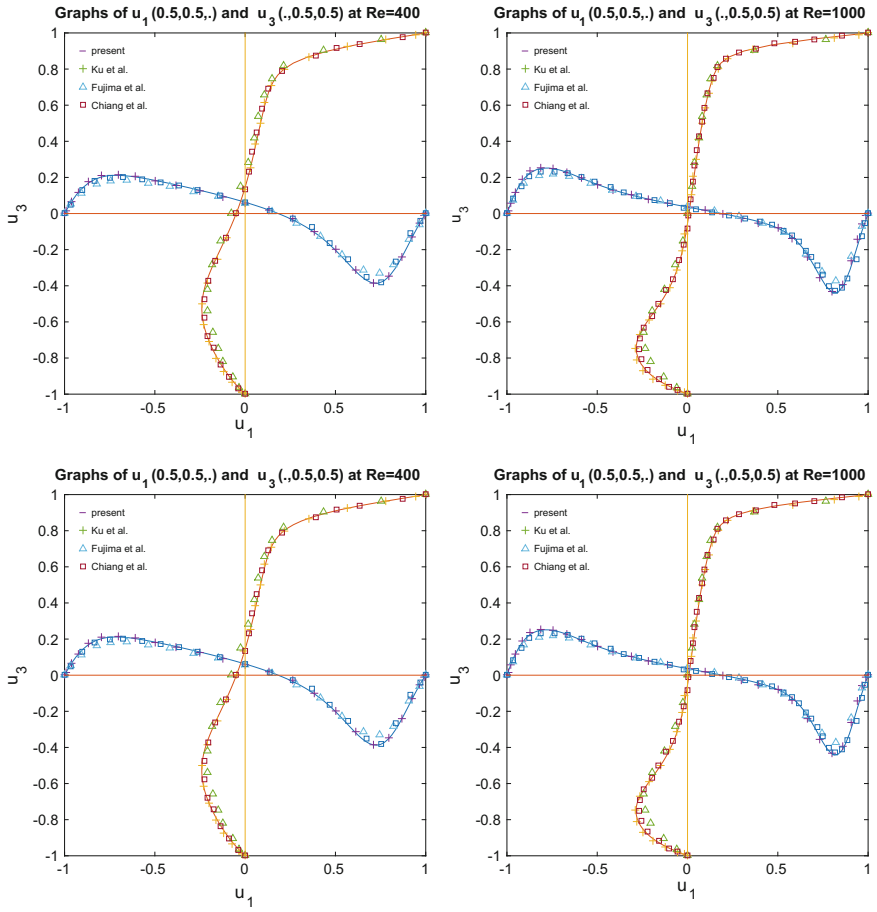

Fig. 1 Comparisons of the numerical results obtained for $h = 1/60$ (top) and 1/96 (bottom) at $\mathrm{Re} = 400$ (left) and 1000 (right)

for the occurrence of the transition is somewhere between 1860 and 1865. Applying a similar analysis, we obtain that, for $h = 1/96$, Re_{cr} is in (1870, 1875), the histories of the velocity L^2-norm being shown in Fig. 3. The oscillation frequencies of the velocity L^2-norm obtained for $h = 1/60$ and $\triangle t = 1/1000$ are about 0.5937 and 0.5941 for $\mathrm{Re} = 1860$ and 1865, respectively. Those obtained for $h = 1/96$ and $\triangle t = 1/1000$ are about 0.5978 and 0.5973 for $\mathrm{Re} = 1870$ and 1875, respectively.

A documented feature of three-dimensional lid-driven cavity flows, like those considered in this section, is that they may exhibit Taylor-Görtler-like (TGL) vortices if Re is sufficiently large. Indeed, Iwatsu, Hyun and Kuwahara reported (in [34]) such vortices at $\mathrm{Re} = 2000$ for cubic cavity flows similar to those considered in this section.

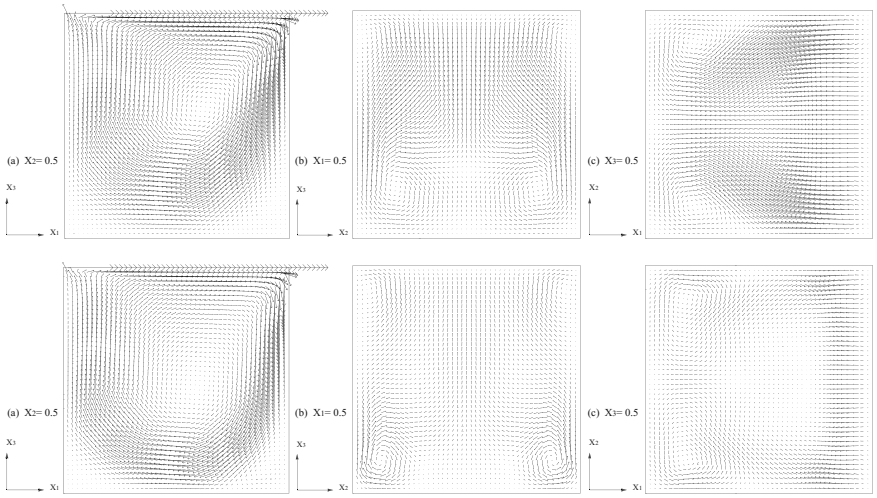

Fig. 2 Steady flow velocity vector of steady flow for Re = 400 (top) and 1000 (bottom) projected on the planes $x_2 = 0.5$ (left), $x_1 = 0.5$ (middle), and $x_3 = 0.5$ (right)

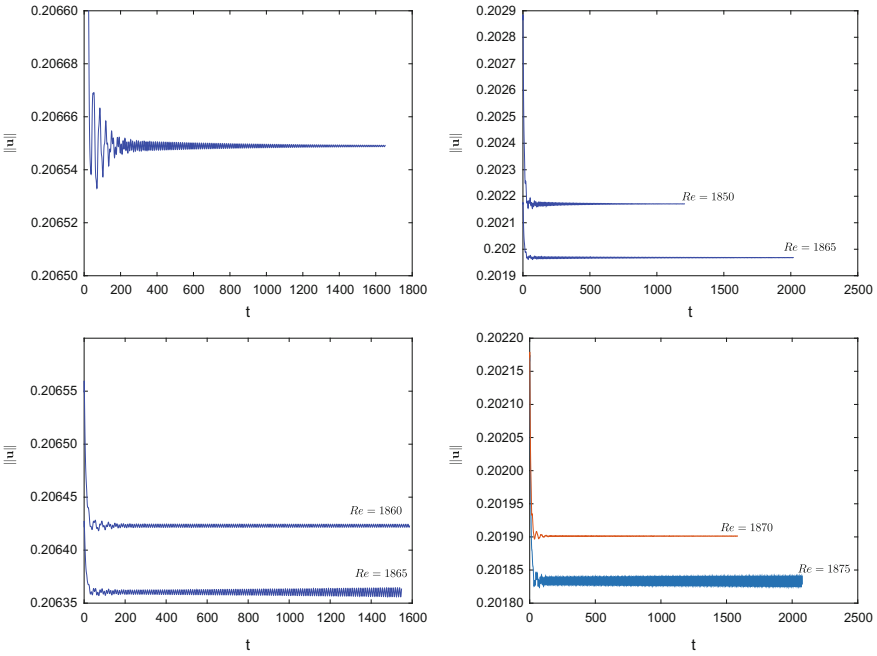

Fig. 3 Histories of the flow field L^2-norm for $h = 1/60$ (left) and 1/96 (right): **a** Re = 1850 (top left), Re = 1860 and 1865 (bottom left); **b** Re = 1850 and 1865 (top right), Re = 1870 and 1875 (bottom right)

Also, as predicted in [16, 41] (and confirmed by our own simulations), a transition from steady flow to oscillatory flow (Hopf bifurcation) occurs at $\mathrm{Re}_{cr} < 2000$. On the other hand, using a global linear stability analysis, Gianetti et al. [19] found that cubic lid-driven cavity flow becomes unstable for Re just above 2000. All these results (ours in particular) lead us to suspect that the Hopf bifurcation is connected to the TGL vortices at Re slightly below 2000.

The bottom left picture of Fig. 3 shows oscillatory regimes at $\mathrm{Re} = 1860$ and 1865, for the flow computed with $h = 1/60$. In order to study the computed flow distortion we have visualized in Figs. 4 (for $\mathrm{Re} = 1860$) and 5 (for $\mathrm{Re} = 1865$) the velocity fields associated with the peak and bottom of the velocity field L^2-norm, and the vector field obtained by difference of the above two velocity fields. The top (resp., bottom) pictures have been obtained by projection of the vector fields on the plane $x_1 = 34/60$ (resp., $x_3 = 1/2$). Figures 4 and 5 show no evidence of TGL vortices for the velocity fields computed with $h = 1/60$ at $\mathrm{Re} = 1860$ and 1865; however, the pictures on the right of Figs. 4 and 5, obtained by the vector field difference detailed above, show a pair of vortices reminiscent of the GTL ones, but with much smaller magnitude since the vector fields have been amplified by a factor of 200 (resp., 50) for $\mathrm{Re} = 1860$

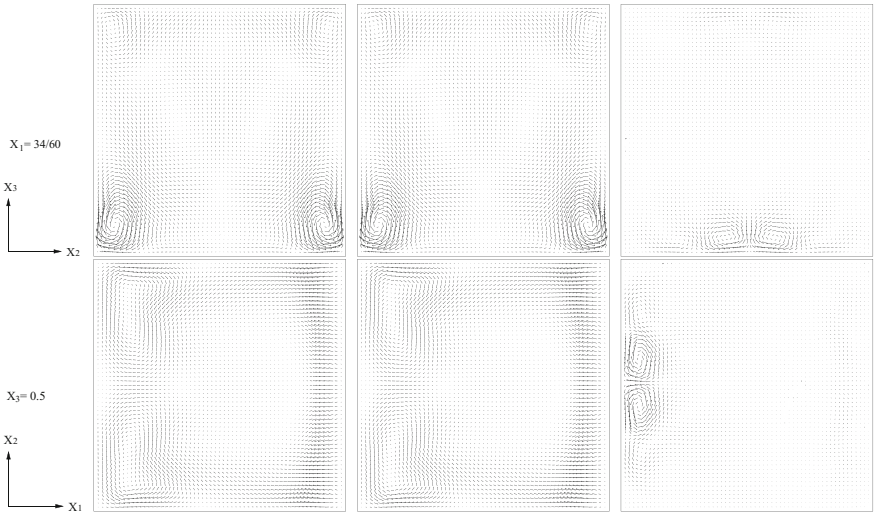

Fig. 4 Left and middle: Projections (at $\mathrm{Re} = 1860$) of the cavity flow velocity vector fields associated with the peak (left) and bottom (middle) of the velocity L^2-norm during an oscillation. Right: Projections (at $\mathrm{Re} = 1860$) of the vector field obtained by difference of the velocity vector fields associated with the peak and bottom of the velocity L^2-norm. All the vector fields are projected on the planes $x_1 = 34/60$ (top) and $x_3 = 0.5$ (bottom). The vector scale for the field obtained by difference (right) is 200 times that of the actual one, while the scale for the two other fields (left and middle) is twice that of the actual one

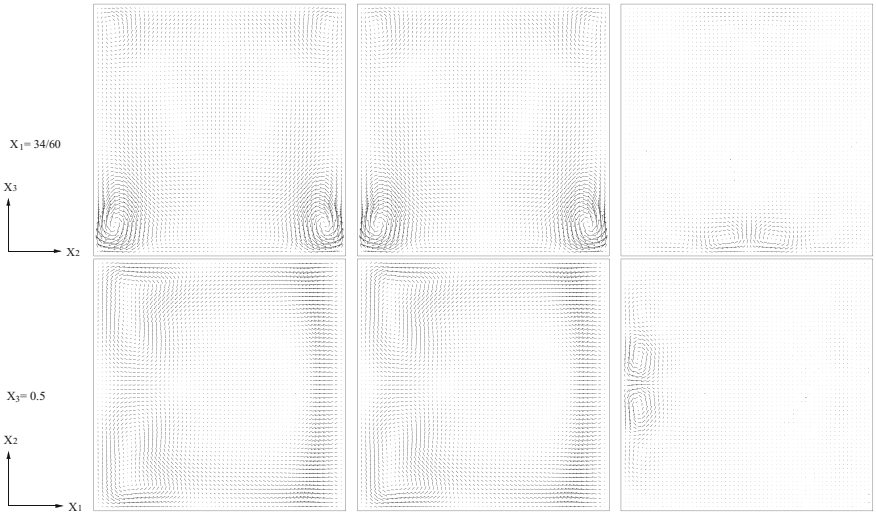

Fig. 5 Left and middle: Projections (at Re = 1865) of the cavity flow velocity vector fields associated with the peak (left) and bottom (middle) of the velocity L^2-norm during an oscillation. Right: Projections (at Re = 1865) of the vector field obtained by difference of the velocity vector fields associated with the peak and bottom of the velocity L^2-norm. All the vector fields are projected on the planes $x_1 = 34/60$ (top) and $x_3 = 0.5$ (bottom). The vector scale for the field obtained by difference (right) is 50 times that of the actual one, while the scale for the two other fields (left and middle) is twice that of the actual one

(resp., 1865) in order to make them visible. On the other hand, at Re = 1875, a pair of TGL vortices becomes visible as shown by Fig. 6 where we have visualized (using a nonlinear scaling to enhance visibility) several snap-shots of the velocity field during an oscillation time period. This pair of TGL vortices is not stationary, however, it remains symmetric with respect to the the mid-plane $x_2 = 1/2$. Figure 6 shows that two tertiary vortices are formed on the left and right parts of the bottom wall, near the large corner vortices at $t = 1526$, 1527 and 1528; next, these tertiary vortices move toward the symmetry plane $x_2 = 0.5$ at $t = 1529$, a pair of TGL vortices being formed in the time interval [1531, 1533]; finally, the TGL vortices disappear after $t = 1533$, to reappear during the next time-period. We have reported on Fig. 7 the projection on the plane $x_1 = 33/60$ of the vector field obtained by difference of the velocity flow fields at $t = 1525$ and $t = 1527$. The vortex pair we observe is reminiscent of those visualized on the right of Figs. 4 and 5. This vortex pair keeps hiding there and becomes stronger as Re increases. These results suggest that the TGL vortices observed for Re slightly below 2000 are related to the onset of an oscillatory flow.

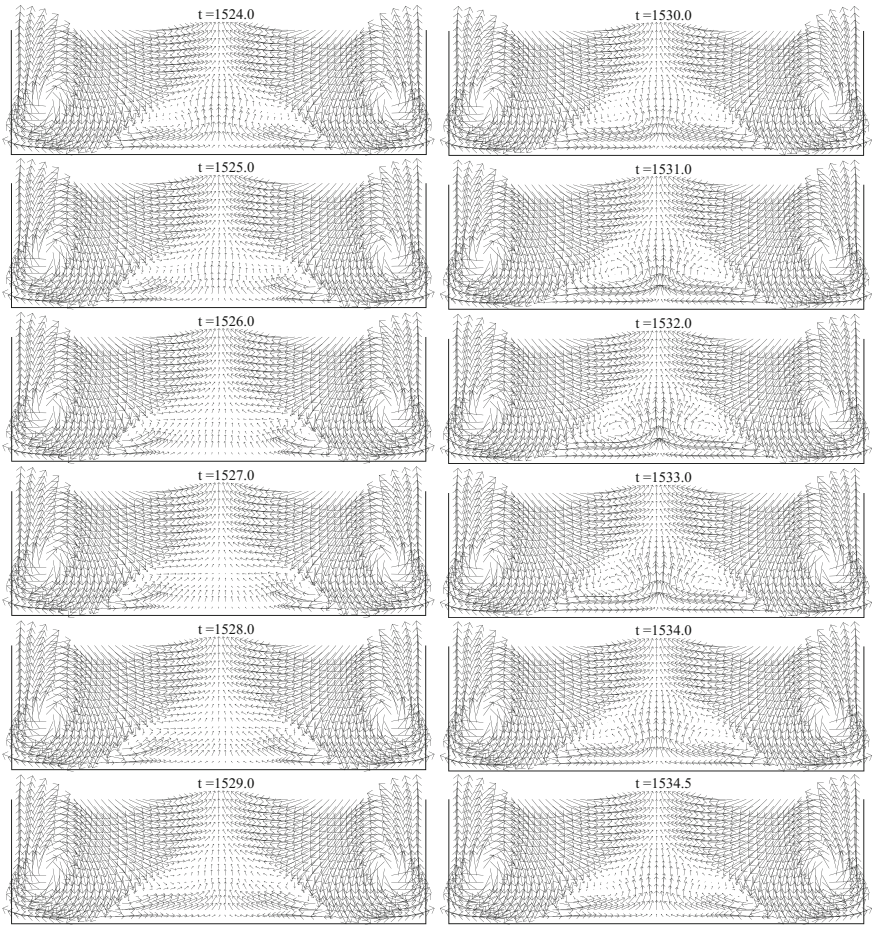

Fig. 6 Projected velocity vector field of the cavity flow at Re = 1875 on the plane $x_1 = 33/60$ at different instants of time during one oscillation of the flow field L^2-norm from $t = 1524$ to 1534.575 [for enhancing the visibility of the TGL vortices we proceeded as follows: (i) for those projected vectors of length ≤ 0.02 the vector scale is 15 times that of the actual one and (ii) for those projected vectors of length > 0.02, the length is reduced to 0.02 first and then plotted as in (i)]

4 Particulate Flow: The Orientation of a Neutrally Buoyant Prolate Ellipsoid in a Three-Dimensional Poiseuille Flow

4.1 Generalities

The distributed Lagrange multiplier/fictitious domain (DLM/FD) formulation for particulate flow, and its associated numerical methodologies based on the Lie scheme have been developed in the past 20 years (see, e.g., [20], Chaps. 8 and 9, [22, 25, 26]). It

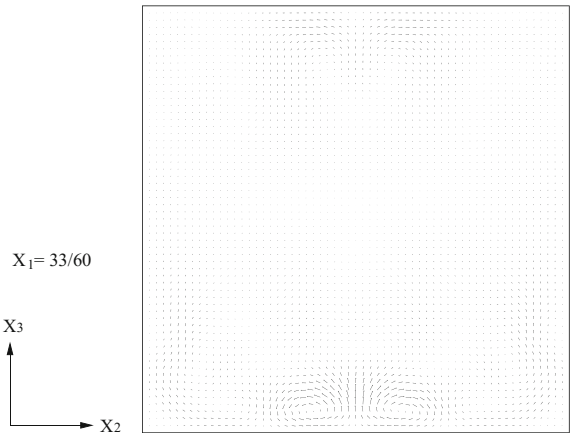

Fig. 7 Projected velocity vector field of the difference of the velocity fields at $t = 1525$ and $t = 1527$ on the plane $x_1 = 33/60$ for $\mathrm{Re} = 1875$. The vector scale is 20 times that of the actual one

is the (necessarily biased) opinion of the authors of this article that the *direct numerical simulation of particulate flow* has been one of the success stories of the wave-like equation-based methodology.

The motion of particles in a channel is relevant to a variety of applications in many chemical engineering and biological processes, such as suspension process, sedimentation, blood flow, and flow cytometry. Understanding this kind of motion has become even more important with the recent advent of microfluidic devices used for many cell-based assays (see, e.g., [33]). The study of the motion of non-spherical particles in viscous fluids has a long history. Jeffery [35] solved the motion of a free ellipsoid for various types of unbounded shear flow under Stokes flow conditions. He concluded that the final state of a spheroid depends on its initial orientation and corresponds to the minimal energy dissipation. The experiments of Segré and Silberberg [54, 55] have had a large influence on fluid mechanics studies of migration and lift of particles. These autohrs studied the migration of dilute suspensions of neutrally buoyant spheres in a tube flow. The particles migrate away from the wall and centerline and accumulate at about 0.6 of the tube radius from the centerline. Karnis et al. [37] verified the same phenomenon and observed, in contrary to Jeffery's theory, that the inertial effect migrates non-spherical particles to a final equilibrium distance in the tube at which the long axis of a rod-like particle rotates within the plane passing through the central axis of the tube and the mass center of the particle; but a disk-like particle will rotates with its short axis perpendicular to the plane passing through the central axis of the tube and the mass center of the disk. In [46], similar migration and rotational behaviors of a neutrally buoyant ellipsoid were obtained at particle Reynolds numbers up to 52; and it was also found that this ellipsoid rotation exhibits distinctive states depending on the Reynolds number range and on the particle shape. In this section, we have further studied the orientation of a prolate ellipsoid in a three-dimensional Poiseuille flow.

4.2 A Fictitious Domain Formulation of the Model Problem

All the fluid-solid interactions to be considered in this article concern the flow of fluid-solid particle mixtures in a cylindrical tube (denoted by **T** in the sequel) with a circular cross-section. In order to take a full advantage of the fictitious domain approach we will embed **T** in a cylindrical tube (denoted by Ω) with a square cross-section whose edge length is slightly larger than the diameter of the **T** cross-section.

We will start our discussion with a one particle situation. Therefore, let $\Omega \subset \mathbb{R}^3$ be a rectangular parallelepiped. We suppose that Ω is filled with a *Newtonian incompressible viscous fluid* (of *density* ρ_f and *viscosity* μ_f) and that it contains a moving neutrally buoyant rigid particle B centered at $\mathbf{G} = \{G_1, G_2, G_3\}^t$ of *density* ρ_f, as shown in Fig. 8, which shows also the inclusion in Ω of the cylinder **T** mentioned above; we suppose that the central axis of both cylinders is parallel to the x_3-axis. The flow is modeled by the *Navier-Stokes equations* while the particle motion is described by the *Euler-Newton equations*. We introduce (with $d\mathbf{x} = dx_1 dx_2 dx_3$) the following functional spaces:

$$W_{0,P} = \{\mathbf{v} \mid \mathbf{v} \in (H^1(\Omega))^3,\ \mathbf{v} = \mathbf{0} \text{ on the top, bottom, front, and back of } \Omega \text{ and } \mathbf{v} \text{ is periodic in the } x_3 \text{ direction}\},$$

$$L^2_0 = \{q \mid q \in L^2(\Omega), \int_\Omega q\, d\mathbf{x} = 0\},$$

$$\Lambda_0(t) = \{\boldsymbol{\mu} \mid \boldsymbol{\mu} \in (H^1(B(t)))^3, \langle \boldsymbol{\mu}, \mathbf{e}_i \rangle_{B(t)} = 0, \langle \boldsymbol{\mu}, \mathbf{e}_i \times \overrightarrow{\mathbf{Gx}} \rangle_{B(t)} = 0,\ i = 1, 2, 3\},$$

$$\Lambda_T = \{\boldsymbol{\mu} \mid \boldsymbol{\mu} \in (H^1(\Omega \setminus \overline{\mathbf{T}}))^3,\ \boldsymbol{\mu} \text{ is periodic in the } x_3 \text{ direction}\},$$

where $\mathbf{e}_1 = \{1, 0, 0\}^t$, $\mathbf{e}_2 = \{0, 1, 0\}^t$, $\mathbf{e}_3 = \{0, 0, 1\}^t$, and $\langle \cdot, \cdot \rangle_{B(t)}$ (resp., $\langle \cdot, \cdot \rangle_T$) is an inner product on $\Lambda_0(t)$ (resp., Λ_T) (see [26], Sect. 5 and [20], Chap. 8) for further information on the choice of $\langle \cdot, \cdot \rangle_{B(t)}$). Above, and from now on, periodicity in the x_3 direction means periodicity of period L, L being the common length of the truncated cylinders Ω and **T**. Then, the distributed Lagrange multiplier based fictitious domain

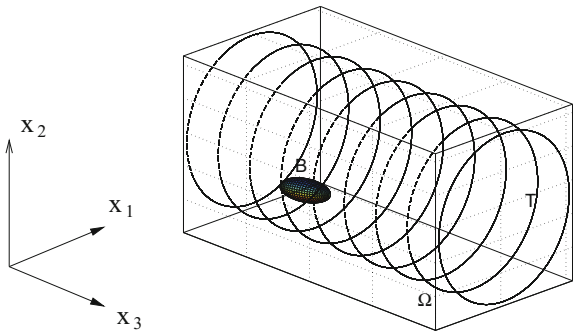

Fig. 8 An example of three-dimensional flow region with one rigid body

formulation for the flow around a freely moving neutrally buoyant particle of general shape inside a cylindrical tube reads as follows (see [20, 50] for a detailed discussion of the non-neutrally buoyant case):

For a.e. $t > 0$, find $\mathbf{u}(t) \in W_{0,P}$, $p(t) \in L^2_0$, $\mathbf{V_G}(t) \in \mathbb{R}^3$, $\mathbf{G}(t) \in \mathbb{R}^3$, $\boldsymbol{\omega}(t) \in \mathbb{R}^3$, $\boldsymbol{\lambda}(t) \in \Lambda_0(t), \boldsymbol{\lambda}_T \in \Lambda_T$ *such that*

$$\begin{cases} \rho_f \displaystyle\int_\Omega \left[\frac{\partial \mathbf{u}}{\partial t} + (\mathbf{u}\cdot\nabla)\mathbf{u}\right]\cdot \mathbf{v}\, d\mathbf{x} + 2\mu_f \int_\Omega \mathbf{D}(\mathbf{u}) : \mathbf{D}(\mathbf{v})\, d\mathbf{x} - \int_\Omega p\nabla\cdot\mathbf{v}\, d\mathbf{x} \\ \quad -\langle \boldsymbol{\lambda}, \mathbf{v}\rangle_{B(t)} - \langle \boldsymbol{\lambda}_T, \mathbf{v}\rangle_T = \rho_f \displaystyle\int_\Omega \mathbf{g}\cdot\mathbf{v}\, d\mathbf{x} + \int_\Omega \mathbf{f}\cdot\mathbf{v}\, d\mathbf{x}, \quad \forall \mathbf{v} \in W_{0,P}, \end{cases} \tag{19}$$

$$\int_\Omega q\nabla\cdot\mathbf{u}(t) d\mathbf{x} = 0, \quad \forall q \in L^2(\Omega), \tag{20}$$

$$\langle \boldsymbol{\mu}, \mathbf{u}(t)\rangle_{B(t)} = 0, \quad \forall \boldsymbol{\mu} \in \Lambda_0(t), \tag{21}$$

$$\langle \boldsymbol{\mu}_T, \mathbf{u}(t)\rangle_T = 0, \quad \forall \boldsymbol{\mu}_T \in \Lambda_T, \tag{22}$$

$$\frac{d\mathbf{G}}{dt} = \mathbf{V_G}, \tag{23}$$

$$\frac{d\mathbf{x}_i}{dt} = \mathbf{V_G} + \boldsymbol{\omega} \times \overrightarrow{\mathbf{G}\mathbf{x}}_i, \quad i = 1, 2, \tag{24}$$

$$\mathbf{V_G}(0) = \mathbf{V_G^0},\ \boldsymbol{\omega}(0) = \boldsymbol{\omega}^0,\ \mathbf{G}(0) = \mathbf{G}^0 = \{G_1^0, G_2^0, G_3^0\}^t,\ \mathbf{x}_i(0) = \mathbf{x}_i^0,\ i = 1, 2, \tag{25}$$

$$\mathbf{u}(\mathbf{x}, 0) = \overline{\mathbf{u}}_0(\mathbf{x}) = \begin{cases} \mathbf{u}_0(\mathbf{x}), & \forall \mathbf{x} \in \Omega \setminus \overline{B(0)}, \\ \mathbf{V_G^0} + \boldsymbol{\omega}^0 \times \overrightarrow{\mathbf{G}^0\mathbf{x}}, & \forall \mathbf{x} \in \overline{B(0)}. \end{cases} \tag{26}$$

In (19)–(26) $\mathbf{u}$ and p denote *velocity* and *pressure*, respectively, $\boldsymbol{\lambda}$ is a *Lagrange multiplier* associated with relation (21) (from (21) the fluid has a rigid body motion in the region occupied by $B(t)$), $\boldsymbol{\lambda}_T$ is a *Lagrange multiplier* associated with relation (22) (from (22), the fluid velocity is $\mathbf{0}$ in $\bar{\Omega} \setminus \mathbf{T}$), $\mathbf{D}(\mathbf{v}) = \frac{1}{2}(\nabla\mathbf{v} + (\nabla\mathbf{v})^t)$, $\mathbf{g}$ denotes *gravity*, $\mathbf{f}$ is an imposed *pressure gradient* pointing in the x_3-direction inside the cylinder $\mathbf{T}$, $\mathbf{V_G}$ is the *translation velocity* of the particle B, and $\boldsymbol{\omega}$ is the *angular velocity* of B. We suppose that the *no-slip* condition holds on ∂B. We also use, if necessary, the notation $\phi(t)$ for the function $\mathbf{x} \to \phi(\mathbf{x}, t)$.

Remark 6 The hydrodynamical forces and torque imposed on the rigid body by the fluid are built in (19)–(26) implicitly (see [26] for details), thus we do not need to compute them explicitly in the simulation. Since in (19)–(26) the flow field is defined on the entire domain Ω, it can be computed with a simple structured grid.

Remark 7 In (21), the rigid body motion in the region occupied by the particle is enforced via Lagrange multipliers $\boldsymbol{\lambda}$. To recover the translation velocity $\mathbf{V_G}(t)$ and the angular velocity $\boldsymbol{\omega}(t)$ from $\mathbf{u}(t)$ satisfying (21), we solve the following equations:

$$\begin{cases} \langle \mathbf{e}_i, \mathbf{u}(t) - \mathbf{V_G}(t) - \boldsymbol{\omega}(t) \times \overrightarrow{\mathbf{Gx}} \rangle_{B(t)} = 0, & \text{for } i = 1, 2, 3, \\ \langle \mathbf{e}_i \times \overrightarrow{\mathbf{Gx}}, \mathbf{u}(t) - \mathbf{V_G}(t) - \boldsymbol{\omega}(t) \times \overrightarrow{\mathbf{Gx}} \rangle_{B(t)} = 0, & \text{for } i = 1, 2, 3. \end{cases} \tag{27}$$

Remark 8 In (24), we have to track the motion of two extra points attached to any particle of general shape so that we can determine the region occupied by the particle via its center of mass, the translation velocity of the center of mass and the angular velocity of the particle. In practice we shall track two orthogonal normalized vectors rigidly attached to the body B from the center of mass $\mathbf{G}$.

Remark 9 In (19), $2\int_\Omega \mathbf{D}(\mathbf{u}) : \mathbf{D}(\mathbf{v})\, d\mathbf{x}$ can be replaced by $\int_\Omega \nabla \mathbf{u} : \nabla \mathbf{v}\, d\mathbf{x}$ since $\mathbf{u}$ is divergence free and in $W_{0,P}$. This change can make the computation simpler and faster. Also the gravity $\mathbf{g}$ in (19) can be absorbed into the pressure term.

Remark 10 The details of numerical methodologies for simulating the motion of prolate and oblate spheroids are given in [46]. Applying Lie's scheme to (19)–(26), we have a six stage operator-splitting scheme, namely: (i) using a L^2-projection Stokes solver à la Uzawa to force the incompressibility condition, (ii) an advection step similar to (4), (iii) a diffusion step with the body force $\mathbf{f}$ and the enforcement of zero velocity outside the cylinder $\mathbf{T}$, (iv) a step to predict the particle position and its orientation, (v) a step to enforce the rigid body motion inside the particle and to obtain its updated translation and angular velocity, and (vi) a step to correct the particle position and its orientation. For the space discretization, we have still used a P_1-*iso*-P_2 (resp., P_1) finite element approximation of the velocity field (resp., pressure) defined from uniform "tetrahedral" meshes $\mathscr{T}_h$ (resp., $\mathscr{T}_{2h}$). For the enforcement of the rigid body motion and zero velocity outside the cylinder, we have applied a collocation method (see [46] for details).

4.3 Numerical Results

For the first series of test problems, we have considered the simulation of a neutrally buoyant prolate ellipsoid moving in a fluid filled cylinder (see Fig. 8). We take $\Omega = (0, 1 + 4h) \times (0, 1 + 4h) \times (0, 2)$ as computational domain with h as the space mesh size to construct the flow velocity spaces. The radius R of the cylinder $\mathbf{T}$ is 0.5 and its length is 2. The semi-long axis of the prolate ellipsoid is 0.195 and its two semi-short axes are 0.065, while the common value of the densities of the fluid and particle is 1. The viscosity of the fluid is $\mu_f = 0.5, 0.1$, or 0.05. The force $\mathbf{f}$ in (19) is a constant vector, positively oriented in the Ox_3 direction; $\|\mathbf{f}\|$ has been chosen so that the maximum velocity of the corresponding *Poiseuille flow* (without particle) is 10. We suppose that

the prolate ellipsoid is at rest initially and that the initial fluid velocity corresponds to the one of a fully developed Poiseuille flow of maximal velocity 10. Thus the Reynolds numbers based on the diameter of the cylinder are $\mathrm{Re} = 10/\mu_f = 20$, 100, and 200, respectively. The initial mass center $\mathbf{G}(0)$ of the ellipsoid is vertically located below the cylinder axis at a distance 0.4 to this axis and the long-axis of the ellipsoid lies on the plane parallel to the x_1x_3-coordinate plane. The initial angle between the long axis and the direction of the x_1-axis has been chosen as 0°, 30°, 60°, or 90°. The one in Fig. 8 corresponds to the case of 90°. We have used uniform tetrahedral meshes to approximate velocity and pressure. The velocity (resp., pressure) mesh size is $h = 1/80$ (resp., $h_p = 2h$), while the time discretization step is $\triangle t = 0.001$.

For all the cases with $\mu_f = 0.5$, the prolate ellipsoid has a tumbling behavior after migrating away from the wall of the cylindrical tube and reaching its equilibrium distance to the central axis of the tube. Its long axis rotates on the plane passing through the cylinder axis and its mass center (e.g., see Fig. 9). The average equilibrium distances of the mass center to the central axis of the tube are 0.5368 R, 0.5396 R, 0.5398 R, and 0.5352 R for the initial angles 0°, 30°, 60°, and 90°, respectively. The particle Reynolds

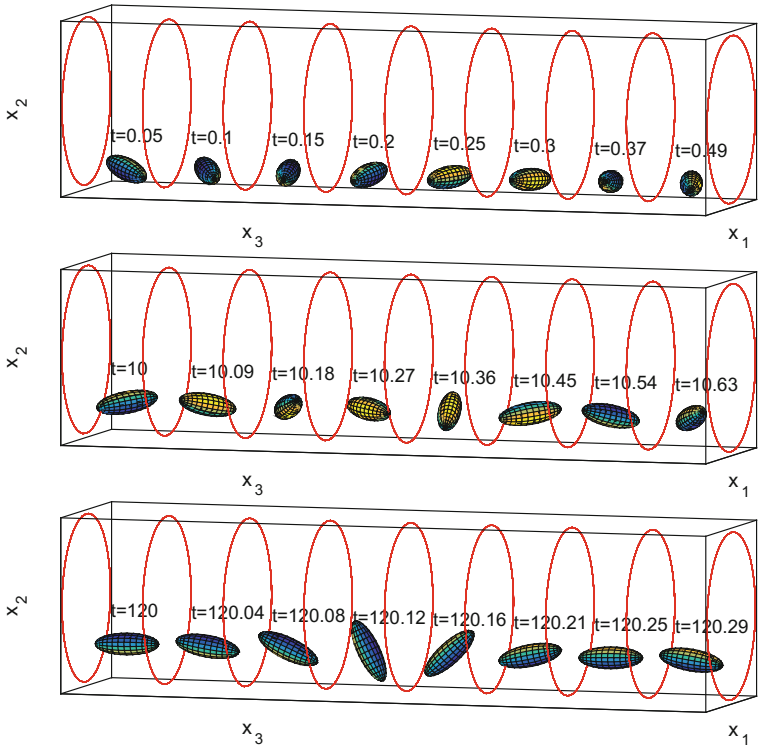

Fig. 9 Visualization of the prolate orientation change from its initial orientation to the rotation with respect to the short axis (tumbling) while reaching its equilibrium distance to the cylinder central axis ($\mu_f = 0.5$, initial angle = 60°)

numbers based on the length of the long axis and the average translation velocity are about 5.4. For all four different initial orientations, the long axis tumbles after it has reached the equilibrium distance to the tube central axis while the center of mass moves along a straight line parallel to the x_3-axis. This behavior is similar to the experimental results of the rod-like particle moving and rotating in the Poiseuille flow reported in [37].

For the cases of $\mu_f = 0.1$, the prolate ellipsoid has two different rotational behaviors after reaching its equilibrium distance to the tube central axis. With the initial angle of 0°, 30° and 60°, the prolate ellipsoid is rotating with respect to its long axis, which is perpendicular to the plane passing through the central axis of the tube and its mass center (see Fig. 10). This motion was not reported in the 1964 paper by Karnis et al. [37], but since this behavior persists after decreasing h and $\triangle t$, the authors strongly believe that it is not a numerical artifact. The average distances of the mass center to the central axis of the tube for both initial angles 0°, 30° and 60° are about 0.519 R for $290 \leq t \leq 300$. Once the center of mass has reached the equilibrium distance to the tube central axis, the ellipsoid does not tumble but rotates with respect to its long axis as

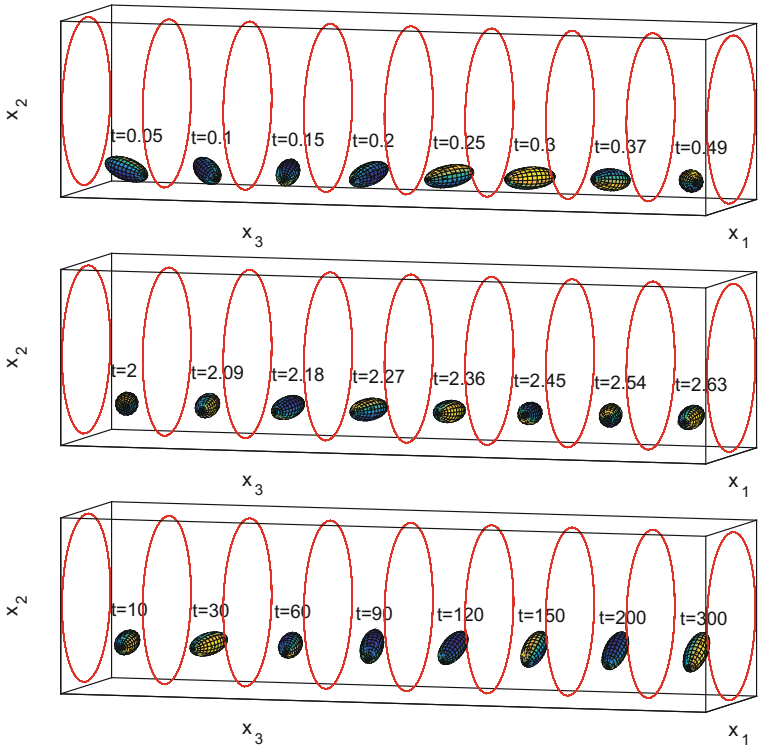

Fig. 10 Visualization of the prolate orientation change from its initial orientation to the rotation with respect to the long axis while reaching its equilibrium distance to the cylinder central axis ($\mu_f = 0.1$, initial angle = 60°)

shown in Fig. 10. The particle Reynolds numbers based on the length of the long-axis and the average translation velocity for $290 \leq t \leq 300$ are about 26.23. For the case of the initial angle equal to 90° (as in Fig. 8), the prolate ellipsoid tumbles just like it does when $\mu_f = 0.5$. For $215 \leq t \leq 225$, the average distance of the mass center to the central axis of the tube is $0.5456\,R$ and the particle Reynolds number is 26.25. The co-existence of two different rotating behaviors at about the same range of Reynolds number is quite unusual. For the two initial angles of 0° and 90°, we have also placed the initial mass center vertically below the cylinder axis at a distance 0.252 to this axis, which is much closer to the cylinder central axis. In both situations, the prolate spheroid migrates away from the cylinder central axis and the rotational motions are eventually the same as those one obtains when the ellipsoid is placed initially closer to the tube boundary.

When decreasing the viscosity to 0.05 and keeping all other parameters the same, we have obtained that, after reaching its equilibrium distance, the prolate spheroid does not tumble but rotate with respect to its long axis for all four different initial angles. But the ellipsoid placed vertically below the cylinder axis at a distance 0.252 to this axis with the initial angles 0° and 90° behaves like it does when $\mu_f = 0.1$.

Thus besides the Reynolds number, the initial distance to the cylinder central axis does matter too. In the near future, we will further study the effect of the initial position and the range of Reynolds number leading to two rotational behaviors.

5 Visco-Elastic Particulate Flow

The motion of particles in non-Newtonian fluids is not only of fundamental theoretical interest, but is also of importance in many applications to industrial processes involving particle-laden materials (see, e.g., [4, 45]). For example, during the hydraulic fracturing operation used in oil and gas wells, suspensions of solid particles in polymeric solutions are pumped into hydraulically-induced fractures. The particles must prop these channels open to enhance the rate of oil recovery [13].

Although numerical methods for simulating particulate flows in Newtonian fluids have been very successful, numerically simulating particulate flows in viscoelastic fluids is much more complicated and challenging. One of the difficulties (e.g., see [2, 38]) for simulating viscoelastic flows is the breakdown of the numerical methods. It has been widely believed that the lack of positive definiteness preserving property of the conformation tensor at the discrete level during the *entire time integration* is one of the reasons for the breakdown. To preserve the positive definiteness property of the conformation tensor, several methodologies have been proposed recently, as in [14, 15, 40, 43]. Lozinski and Owens [43] factored the conformation tensor to get $\boldsymbol{\sigma} = AA^T$ and then they wrote down the equations for A approximately at the discrete level. Hence, the positive definiteness of the conformation tensor is forced with such an

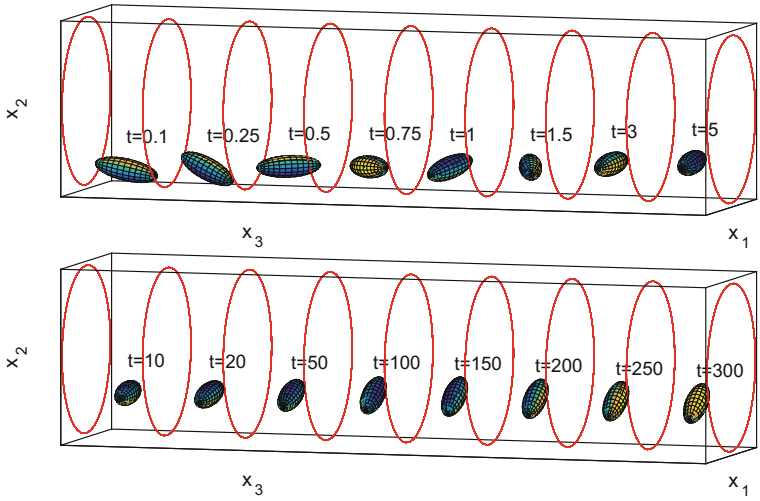

Fig. 11 Visualization of the change of orientation of the prolate ellipsoid: From its initial orientation to its rotation around its long axis, while reaching an equilibrium distance to the axis of the cylinder ($\mu_f = 0.05$, initial angle $= 90°$)

approach. The methodologies developed in [43] have been applied in [29] together with the FD/DLM method through operator splitting techniques for simulating particulate flows in Oldroyd-B fluid. We have generalized these computational methodologies to viscoelastic fluids of the FENE-CR type, which is a more "realistic" model when compared with the Oldroyd-B model as advocated in [53]. We have compared the particle sedimenting in a vertical two-dimensional channel filled with viscoelastic fluid of either Oldroyd-B or FENE-CR type to find out the effect of the maximum extension of the immersed polymer coils on the chaining (Fig. 11).

5.1 Mathematical Formulations

Following the work developed in [29], we will first address in the following the models and computational methodologies combined with the Lozinski and Owens' factorization approach. Let Ω be a bounded domain in $\mathbb{R}^d$ ($d = 2$ or 3) and let Γ be the boundary of Ω. We suppose that Ω is filled with a viscoelastic fluid of either Oldroyd-B or FENE-CR type of density ρ_f and that it contains N moving rigid particles of density ρ_s (see Fig. 12).

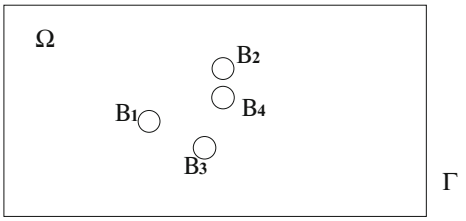

Fig. 12 An example of a two-dimensional flow region with four circular particles

Let $B(t) = \cup_{i=1}^{N} B_i(t)$ where $B_i(t)$ is the ith rigid particle in the fluid for $i = 1, \ldots, N$. We denote by $\partial B_i(t)$ the boundary of $B_i(t)$ for $i = 1, \ldots, N$. For some $T > 0$, the governing equations for the fluid-particle system are

$$\rho_f \left(\frac{\partial \mathbf{u}}{\partial t} + (\mathbf{u} \cdot \nabla)\mathbf{u} \right) = \rho_f \mathbf{g} - \nabla p + 2\mu \nabla \cdot \mathbf{D}(\mathbf{u}) + \nabla \cdot \boldsymbol{\sigma}^p \text{ in } \Omega \setminus \overline{B(t)},\ t \in (0, T), \tag{28}$$

$$\nabla \cdot \mathbf{u} = 0 \quad \text{in } \Omega \setminus \overline{B(t)},\ t \in (0, T), \tag{29}$$

$$\mathbf{u}(\mathbf{x}, 0) = \mathbf{u}_0(\mathbf{x}), \quad \forall \mathbf{x} \in \Omega \setminus \overline{B(0)}, \quad \text{with } \nabla \cdot \mathbf{u}_0 = 0, \tag{30}$$

$$\mathbf{u} = \mathbf{g}_0 \quad \text{on } \Gamma \times (0, T), \quad \text{with } \int_{\Gamma} \mathbf{g}_0 \cdot \mathbf{n}\, d\Gamma = 0, \tag{31}$$

$$\mathbf{u} = \mathbf{V}_{p,i} + \boldsymbol{\omega}_i \times \overrightarrow{\mathbf{G}_i \mathbf{x}}, \quad \forall \mathbf{x} \in \partial B_i(t), \quad i = 1, \ldots, N, \tag{32}$$

$$\frac{\partial \mathbf{C}}{\partial t} + (\mathbf{u} \cdot \nabla)\mathbf{C} - (\nabla \mathbf{u})\mathbf{C} - \mathbf{C}(\nabla \mathbf{u})^t = -\frac{f(\mathbf{C})}{\lambda_1}(\mathbf{C} - \mathbf{I}) \text{ in } \Omega \setminus \overline{B(t)},\ t \in (0, T), \tag{33}$$

$$\mathbf{C}(\mathbf{x}, 0) = \mathbf{C}_0(\mathbf{x}), \quad \mathbf{x} \in \Omega \setminus \overline{B(0)}, \tag{34}$$

$$\mathbf{C} = \mathbf{C}_L, \quad \text{on } \Gamma^-, \tag{35}$$

where $\mathbf{u}$ is the flow velocity, p is the pressure, $\mathbf{g}$ is the gravity, $\mu = \eta_1 \lambda_2 / \lambda_1$ is the Newtonian viscosity of the fluid, $\eta = \eta_1 - \mu$ is the elastic viscosity of the fluid, η_1 is the fluid viscosity, λ_1 is the relaxation time of the fluid, λ_2 is the retardation time of the fluid, $\mathbf{n}$ is the outer normal unit vector at Γ, Γ^- is the upstream portion of Γ. The polymeric stress tensor $\boldsymbol{\sigma}^p$ in (28) is given by $\boldsymbol{\sigma}^p = \frac{\eta}{\lambda_1} f(\mathbf{C})(\mathbf{C} - \mathbf{I})$, where the conformation tensor $\mathbf{C}$ is symmetric and positive definite (see [36]) and $\mathbf{I}$ is the identity matrix. Setting f equal to unity corresponds to the Oldroyd-B model while

$$f(\mathbf{C}) = \frac{L^2}{L^2 - tr(\mathbf{C})} \tag{36}$$

corresponds to the FENE-CR model [6], where $tr(\mathbf{C})$ is the trace of the conformation tensor $\mathbf{C}$ and L is the maximum extension of the immersed polymer coils and referred to as the extensibility of the immersed polymer coils. The Oldroyd-B model then is a special case associated with infinite extensibility.

In (32), the no-slip condition holds on the boundary of the ith particle, $\mathbf{V}_{p,i}$ is the translation velocity, $\boldsymbol{\omega}_i$ is the angular velocity and $\mathbf{G}_i$ is the center of mass. The motion of the particles is modeled by Newton's laws:

$$M_{p,i}\frac{d\mathbf{V}_{p,i}}{dt} = M_{p,i}\mathbf{g} + \mathbf{F}_i + \mathbf{F}_i^r, \tag{37}$$

$$\frac{d(\mathbf{I}_{p,i}\boldsymbol{\omega}_i)}{dt} = \mathbf{F}_i^t, \tag{38}$$

$$\frac{d\mathbf{G}_i}{dt} = \mathbf{V}_{p,i}, \tag{39}$$

$$\mathbf{G}_i(0) = \mathbf{G}_i^0, \quad \mathbf{V}_{p,i}(0) = \mathbf{V}_{p,i}^0, \quad \boldsymbol{\omega}_i(0) = \boldsymbol{\omega}_i^0, \tag{40}$$

for $i = 1, \ldots, N$, where in (37)–(40), $M_{p,i}$ and $\mathbf{I}_{p,i}$ are the the mass and the inertia tensor of the ith particle, respectively, $\mathbf{F}_i^r$ is a short range repulsion force imposed on the ith particle by other particles and the wall to prevent particle/particle and particle/wall penetration (see [26] for details), and $\mathbf{F}_i$ and $\mathbf{F}_i^t$ denote the hydrodynamic force and the associated torque imposed on the ith particle by the fluid, respectively.

To avoid the frequent remeshing and the difficulty of the mesh generation for a time-varying domain in which the rigid particles can be very close to each other, especially for three dimensional particulate flow, we have extended the governing equations to the entire domain Ω (a fictitious domain). For a fictitious-domain-based variational formulation of the governing equations of the particulate flow, we consider only one rigid particle $B(t)$ (either a disk in 2D or a ball in 3D) in the fluid domain without losing generality. Let us define first the following functional spaces

$$\begin{aligned}
\mathbf{V}_{\mathbf{g}_0(t)} &= \{\mathbf{v} \mid \mathbf{v} \in (H^1(\Omega))^d,\ \mathbf{v} = \mathbf{g}_0(t) \text{ on } \Gamma\},\\
L_0^2(\Omega) &= \{q \mid q \in L^2(\Omega),\ \int_\Omega q\, d\mathbf{x} = 0\},\\
\mathbf{V}_{\mathbf{C}_L(t)} &= \{\mathbf{C} \mid \mathbf{C} \in (H^1(\Omega))^{d\times d},\ \mathbf{C} = \mathbf{C}_L(t) \text{ on } \Gamma^-\},\\
\mathbf{V}_{\mathbf{C}_0} &= \{\mathbf{C} \mid \mathbf{C} \in (H^1(\Omega))^{d\times d},\ \mathbf{C} = 0 \text{ on } \Gamma^-\},\\
\Lambda(t) &= H^1(B(t))^d.
\end{aligned}$$

Following the methodologies developed in [26, 56], a fictitious domain formulation of the governing Eqs. (28)–(40) reads as follows:

For a.e. $t > 0$, *find* $\mathbf{u}(t) \in \mathbf{V}_{\mathbf{g}_0(t)}$, $p(t) \in L^2_0(\Omega)$, $\mathbf{C}(t) \in \mathbf{V}_{\mathbf{C}_L(t)}$, $\mathbf{V}(t) \in \mathbb{R}^d$, $\mathbf{G}(t) \in \mathbb{R}^d$, $\boldsymbol{\omega}(t) \in \mathbb{R}^d$, $\boldsymbol{\lambda}(t) \in \Lambda(t)$ *such that*

$$\begin{cases} \rho_f \displaystyle\int_\Omega \left[\frac{\partial \mathbf{u}}{\partial t} + (\mathbf{u}\cdot\nabla)\mathbf{u}\right]\cdot \mathbf{v}\, d\mathbf{x} + 2\mu \int_\Omega \mathbf{D}(\mathbf{u}) : \mathbf{D}(\mathbf{v})\, d\mathbf{x} - \int_\Omega p\nabla\cdot\mathbf{v}\, d\mathbf{x} \\ - \displaystyle\int_\Omega \mathbf{v}\cdot(\nabla\cdot\boldsymbol{\sigma}^p)\, d\mathbf{x} + (1-\rho_f/\rho_s)\left\{M_p\frac{d\mathbf{V}}{dt}\cdot\mathbf{Y} + \mathbf{I}_p\frac{d\boldsymbol{\omega}}{dt}\cdot\boldsymbol{\theta}\right\} \\ -\langle \boldsymbol{\lambda}, \mathbf{v} - \mathbf{Y} - \boldsymbol{\theta}\times\overrightarrow{\mathbf{Gx}}\rangle_{B(t)} - \mathbf{F}^r\cdot\mathbf{Y} \\ = \rho_f \displaystyle\int_\Omega \mathbf{g}\cdot\mathbf{v} d\mathbf{x} + (1-\rho_f/\rho_s)M_p\mathbf{g}\cdot\mathbf{Y}, \\ \forall\{\mathbf{v},\mathbf{Y},\boldsymbol{\theta}\} \in (H^1_0(\Omega))^d \times \mathbb{R}^d \times \mathbb{R}^d, \end{cases} \tag{41}$$

$$\int_\Omega q\nabla\cdot\mathbf{u}(t)\, d\mathbf{x} = 0, \forall q \in L^2(\Omega), \tag{42}$$

$$\langle \boldsymbol{\mu}, \mathbf{u}(\mathbf{x},t) - \mathbf{V}(t) - \boldsymbol{\omega}(t)\times\overrightarrow{\mathbf{G}(t)\mathbf{x}}\rangle_{B(t)} = 0, \ \forall \boldsymbol{\mu} \in \boldsymbol{\Lambda}(t), \tag{43}$$

$$\int_\Omega \left(\frac{\partial \mathbf{C}}{\partial t} + (\mathbf{u}\cdot\nabla)\mathbf{C} - (\nabla\mathbf{u})\mathbf{C} - \mathbf{C}(\nabla\mathbf{u})^t\right) : \mathbf{s}\, d\mathbf{x} \tag{44}$$

$$= -\int_\Omega \frac{f(\mathbf{C})}{\lambda_1}(\mathbf{C}-\mathbf{I}) : \mathbf{s}\, d\mathbf{x}, \quad \forall \mathbf{s} \in \mathbf{V}_{\mathbf{C}_0}, \text{ with } \mathbf{C} = \mathbf{I} \text{ in } B(t),$$

$$\frac{d\mathbf{G}}{dt} = \mathbf{V}, \tag{45}$$

$$\mathbf{C}(\mathbf{x},0) = \mathbf{C}_0(\mathbf{x}), \quad \forall \mathbf{x} \in \Omega, \text{ with } \mathbf{C}_0 = \mathbf{I} \text{ in } B(0), \tag{46}$$

$$\mathbf{G}(0) = \mathbf{G}_0, \quad \mathbf{V}(0) = \mathbf{V}_0, \quad \boldsymbol{\omega}(0) = \boldsymbol{\omega}_0, \quad B(0) = B_0, \tag{47}$$

$$\mathbf{u}(\mathbf{x},0) = \begin{cases} \mathbf{u}_0(\mathbf{x}), & \forall \mathbf{x} \in \Omega \setminus \overline{B_0}, \\ \mathbf{V}_0 + \boldsymbol{\omega}_0 \times \overrightarrow{\mathbf{G}_0\mathbf{x}}, & \forall \mathbf{x} \in \overline{B_0}. \end{cases} \tag{48}$$

In (41) the *Lagrange multiplier* $\boldsymbol{\lambda}$ defined over B can be viewed as an extra body force maintaining the rigid body motion inside B. The conformation tensor $\mathbf{C}$ inside the rigid particle is extended as the identity tensor $\mathbf{I}$ as in (44) since the polymeric stress tensor is zero inside the rigid particle. In Eq. (41), since $\mathbf{u}$ is divergence free and satisfies the Dirichlet boundary conditions on Γ, we have $2\int_\Omega \mathbf{D}(\mathbf{u}) : \mathbf{D}(\mathbf{v})d\mathbf{x} = \int_\Omega \nabla\mathbf{u} : \nabla\mathbf{v}d\mathbf{x}$, $\forall \mathbf{v} \in (H^1_0(\Omega))^d$. This is a substantial simplification from the computational point of view, which is another advantage of the fictitious domain approach. With this simplification, we can use, as shown in the following section, fast solvers for the elliptic problems in order to speed up computations. Also the gravity term $\mathbf{g}$ in (41) can be absorbed in the pressure term.

5.2 Numerical Results

The details of numerical methodologies for simulating the motion of disks sedimenting in Oldroyd-B fluid in a vertical two-dimensional channel are given in [29]. Applying Lie's scheme to (41)–(48), we have used a six-stage operator-splitting scheme, namely:

Stage 1 We use a Neumann preconditioned Uzawa/conjugate gradient algorithm to force (in a L^2 sense) the incompressibility condition of $\mathbf{u}$.
Stage 2 We combine two advection steps similar to (4): one for $\mathbf{u}$ and one for $\mathbf{C}$.
Stage 3 We combine a diffusion step for $\mathbf{u}$ with a step taking into account the remaining operator in the evolution equation verified by $\mathbf{C}$.
Stage 4 We update the position of $\mathbf{G}$.
Stage 5 We force the rigid body motion of the particle, update $\mathbf{V}$ and $\boldsymbol{\omega}$, and impose the condition $\mathbf{C} = \mathbf{I}$ inside the particle.
Stage 6 This is a diffusion step for the velocity, driven by the updated polymeric stress tensor.

We present here the results of two numerical experiments concerning the sedimentation of circular particles in a two-dimensional channel filled with an Oldroyd-B fluid. For the space discretization, we have still used a P_1-*iso*-P_2 (resp., P_1) finite element for the approximation of velocity field (resp., pressure) defined from uniform "triangular" meshes $\mathscr{T}_h$ (resp., $\mathscr{T}_{2h}$). For the finite element approximation of each entry in the conformation tensor, P_1 finite element spaces defined from uniform triangular meshes $\mathscr{T}_h$ have been used. For the enforcement of the rigid body motion, we have applied a collocation method (see [26] for details).

The numerical results concern six circular particles of diameter $D = 0.25$ sedimenting in a channel filled with an Oldroyd-B fluid. The channel is infinitely long and has a width of 1. The computational domain is $\Omega = (0, 1) \times (0, 7)$ initially and then moves down with the mass center of the lowest of the six particles. It is known that when the elasticity number $\mathrm{E} = \mathrm{De}/\mathrm{Re}$ is larger than the critical value ($O(1)$) and the Mach number $\mathrm{M} = \sqrt{\mathrm{DeRe}} < 1$, the particles in this case will form chains that are parallel to the flow [32, 42]. In our simulations, all six particles are lined up along the flow direction, agreeing thus the known observations and experiments. Figure 13 gives the snapshots at various moments of time of the particles lining up phenomenon.

We can see that, after drafting, kissing and chaining, the six particles form approximately a straight line at $t = 20$; at $t = 30$, the trailing particle has been separated from the leading five particles. This observation agrees with experiments showing that, sometimes, the last particle in the chain gets detached as discussed in [51]. It is known that a long chain falls faster than a single particle in the fluid. This long body effect tends to detach the last particle from the chain. The average terminal velocity is 0.1535 for $26 \leq t \leq 30$, the Reynolds number is $\mathrm{Re} = 0.1476$, the Deborah number is $\mathrm{De} = 0.7981$, the elasticity number is $\mathrm{E} = 5.408$ and the Mach number is $\mathrm{M} = 0.3432$. With the same parameters as in the case of Oldroyd-B fluid, we just changed to the FENE-CR model with $L = 5$ for the polymer extension limit. Since the viscoelastic fluid has a shorter polymer extension limit, it cannot hold all six disks together as shown in Fig. 14. For this case, the average terminal velocity is 0.1317 for

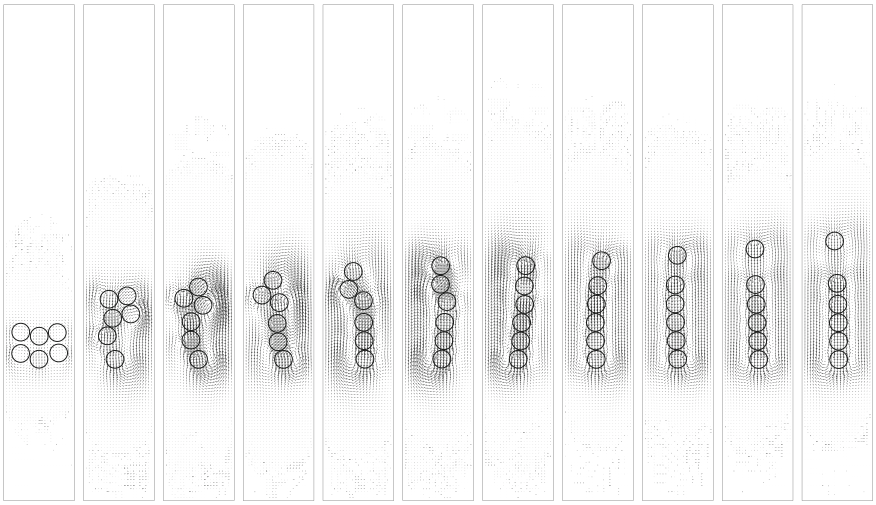

Fig. 13 Snapshots at $t = 2, 10, 12, 14, 16, 18, 20, 24, 26, 28$, and 30 of the positions of six particles lining up in an Oldroyd-B fluid ($h = 1/96$ and $\triangle t = 0.0004$)

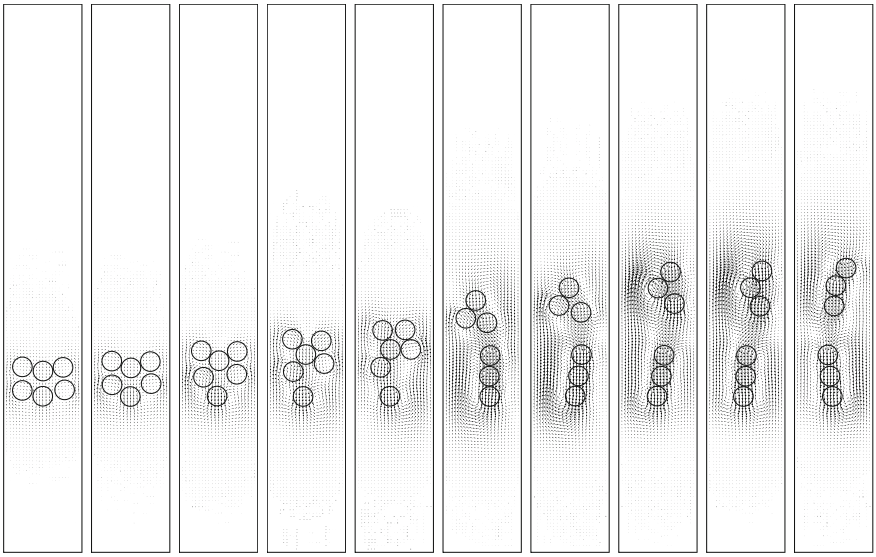

Fig. 14 Snapshots at $t = 2, 4, 6, 8, 10, 18, 20, 24, 26$, and 30 of the positions of six particles lining up in an FENE-CR fluid with $L = 5$ ($h = 1/96$ and $\triangle t = 0.0004$)

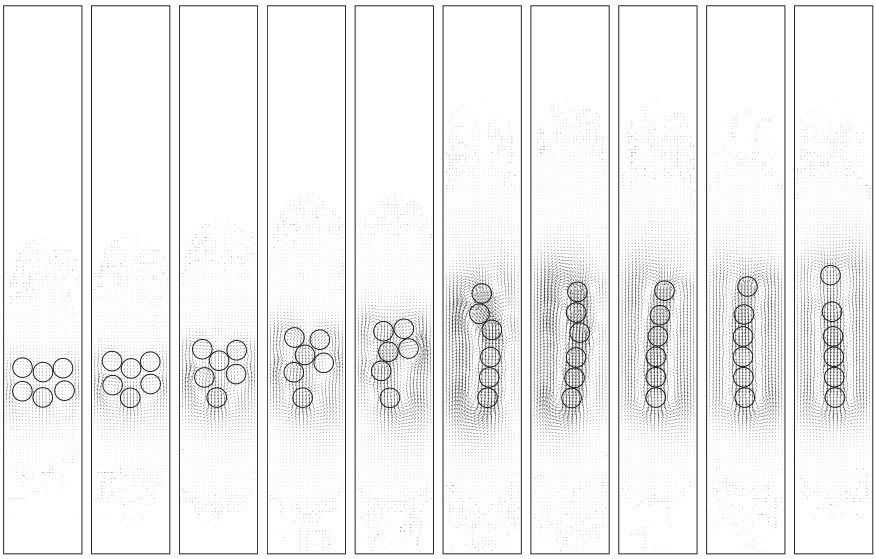

Fig. 15 Snapshots at $t = 2, 4, 6, 8, 10, 18, 20, 24, 26$, and 30 of the positions of six particles lining up in an FENE-CR fluid with $L = 10$ ($h = 1/96$ and $\triangle t = 0.0004$)

$26 \leq t \leq 30$, and the associated numbers are $\mathrm{Re} = 0.1266$, $\mathrm{De} = 0.6847$, $\mathrm{E} = 5.408$ and $\mathrm{M} = 0.2944$. But for the case $L = 10$, the chaining shown in Fig. 15 is much closer to the one obtained for the Oldroyd-B fluid since in (36), $f(\mathbf{C})$ is close to 1 (i.e., the FENE-CR model has almost recovered the Oldroyd-B model). The terminal velocity is 0.1490 for $26 \leq t \leq 30$, and the associated numbers are $\mathrm{Re} = 0.1433$, $\mathrm{De} = 0.7750$, $\mathrm{E} = 5.408$ and $\mathrm{M} = 0.3333$.

6 Conclusion

The wave-like equation based method we introduced twenty years ago, for the numerical simulation of incompressible viscous flow (as an alternative to Lagrange-Galerkin methods) has been further discussed in this article. This method, which allows a purely variational treatment of the advection (well-suited to simple finite element approximations), has been briefly described in Sect. 2 of this article, and applied in Sects. 3–5 to the simulation of Newtonian and non-Newtonian viscous flows in two and three dimensions, possibly involving rigid solid particles. Through the methodology discussed in this article we have been able to reproduce accurately documented phenomena from the physics of fluids, and more importantly to discover new ones, as shown in Sects. 4 and 5. The results reported in this article suggest that, despite being twenty years old, the methodology we discussed in this article is far from being obsolete and should be still helpful in the future.

Acknowledgements The authors of this article are thanking the editors of this volume, a very special thank being due to Marja-Leena Rantalainen, from the University of Jyväskylä in Finland, for her beautiful processing of this contribution. The support of the US National Science Foundation via grant DMS-1418308 is also acknowledged.

References

1. Anupindi K, Lai W, Frankel S (2014) Characterization of oscillatory instability in lid driven cavity flows using lattice Boltzmann method. Comput Fluids 92:7–21
2. Baaijens FPT (1998) Mixed finite element methods for viscoelastic flow analysis: a review. J Non-Newton Fluid Mech 79(2–3):361–385
3. Bristeau MO, Glowinski R, Périaux J (1987) Numerical methods for the Navier-Stokes equations. Application to the simulation of compressible and incompressible viscous flow. Comput Phys Rep 6:73–187
4. Chhabra RP (1993) Bubbles, drops, and particles in non-Newtonian fluids. CRC Press, Boca Raton, FL
5. Chiang TP, Sheu WH, Hwang RR (1998) Effect of Reynolds number on the eddy structure in a lid-driven cavity. Int J Numer Meth Fluids 26(5):557–579
6. Chilcott MD, Rallison JM (1988) Creeping flow of dilute polymer solutions past cylinders and spheres. J Non-Newton Fluid Mech 29:381–432
7. Chippada S, Dawson CN, Martinez ML, Wheeler MF (1998) Finite element approximations to the system of shallow water equations I: continuous-time a priori error estimates. SIAM J Numer Anal 35(2):692–711
8. Chippada S, Dawson CN, Martínez-Canales ML, Wheeler MF (1998) Finite element approximations to the system of shallow water equations, Part II: discrete-time a priori error estimates. SIAM J Numer Anal 36(1):226–250
9. Chorin AJ (1967) A numerical method for solving incompressible viscous flow problems. J Comput Phys 2(1):12–26
10. Dean EJ, Glowinski R (1997) A wave equation approach to the numerical solution of the Navier-Stokes equations for incompressible viscous flow. CR Acad Sci Paris Sér I Math 325(7):783–791
11. Dean EJ, Glowinski R, Guidoboni G (2007) On the numerical simulation of Bingham visco-plastic flow: old and new results. J Non-Newton Fluid Mech 142(1–3):36–62
12. Dean EJ, Glowinski R, Pan T-W (1998) A wave equation approach to the numerical simulation of incompressible viscous fluid flow modelled by the Navier-Stokes equations. In: De Santo JA (ed) Mathematical and numerical aspects of wave propagation (Golden. CO, 1998). Philadelphia, PA, pp 65–74
13. Economides MJ, Nolte KG (1989) Reservoir stimulation. Prentice Hall, Englewood Cliffs, NJ
14. Fattal R, Kupferman R (2004) Constitutive laws for the matrix-logarithm of the conformation tensor. J Non-Newton Fluid Mech 123(2–3):281–285
15. Fattal R, Kupferman R (2005) Time-dependent simulation of viscoelastic flows at high Weissenberg number using the log-conformation representation. J Non-Newton Fluid Mech 126(1):23–37
16. Feldman Y, Gelfgat AY (2010) Oscillatory instability of a three-dimensional lid-driven flow in a cube. Phys Fluids 22:093602
17. Fujima S, Tabata M, Fukasawa Y (1994) Extension to three-dimensional problems of the upwind finite element scheme based on the choice of up- and downwind points. Comput Methods Appl Mech Eng. 112:109–131
18. Ghia UK, Ghia KN, Shin CT (1982) High-Re solutions for incompressible flow using the Navier-Stokes equations and a multigrid method. J Comput Phys 48(3):387–411
19. Giannetti R, Luchini P, Marino L (2009) Linear stability analysis of three-dimensional lid-driven cavity flow. In: Atti del XIX Congresso AIMETA di Meccanica Teorica e Applicata (Ancona, 2009), Aras Edizioni, pp 738.1–738.10

20. Glowinski R (2003) Finite element methods for incompressible viscous flow. In: Ciarlet PG, Lions JL (eds) Handbook of numerical analysis, vol IX. North-Holland, Amsterdam, pp 3–1176
21. Glowinski R (2015) Variational methods for the numerical solution of nonlinear elliptic problems. SIAM, Philadelphia, PA
22. Glowinski R, Dean EJ, Guidoboni G, Juárez LH, Pan T-W (2008) Applications of operator-splitting methods to the direct numerical simulation of particulate and free-surface flows and to the numerical solution of the two-dimensional elliptic Monge-Ampère equation. Jap J Indust Appl Math 25(1):1–63
23. Glowinski R, Guidoboni G, Pan T-W (2006) Wall-driven incompressible viscous flow in a two-dimensional semi-circular cavity. J Comput Phys 216(1):76–91
24. Glowinski R, Lawton W, Ravachol M, Tenenbaum E (1990) Wavelet solution of linear and nonlinear elliptic, parabolic and hyperbolic problems in one space dimension. In: Glowinski R, Lichnewsky A (eds) Computing methods in applied sciences and engineering (Paris, 1990). SIAM, Philadelphia, PA, pp 55–120
25. Glowinski R, Osher S, Yin W (eds) (2016) Splitting methods in communication and imaging, science and engineering. Springer, New York
26. Glowinski R, Pan T-W, Hesla TI, Joseph DD, Périaux J (2001) A fictitious domain approach to the direct numerical simulation of incompressible viscous flow past moving rigid bodies: application to particulate flow. J Comput Phys 169(2):363–426
27. Glowinski R, Wachs A (2011) On the numerical simulation of viscoplastic fluid flow. In: Ciarlet PG, Glowinski R, Xu J (eds) Handbook of numerical analysis, vol XVI. North-Holland, Amsterdam, pp 483–718
28. Gustafsson B, Kreiss H-O, Oliger J (1995) Time dependent problems and difference methods. Wiley, New York
29. Hao J, Pan T-W, Glowinski R, Joseph DD (2009) A fictitious domain/distributed Lagrange multiplier method for the particulate flow of Oldroyd-B fluids: a positive definiteness preserving approach. J Non-Newton Fluid Mech 156(1–2):95–111
30. He Q, Glowinski R, Wang XP (2011) A least-squares/finite element method for the numerical solution of the Navier-Stokes-Cahn-Hilliard system modeling the motion of the contact line. J. Comput. Phys. 230(12):4991–5009
31. Hou S, Pan T-W, Glowinski R (2014) Circular band formation for incompressible viscous fluid-rigid-particle mixtures in a rotating cylinder. Phys Rev E 89(2):023013
32. Huang PY, Hu HH, Joseph DD (1998) Direct simulation of the sedimentation of elliptic particles in Oldroyd-B fluids. J Fluid Mech 362:297–326
33. Hur SC, Choi SE, Kwon S, Di Carlo D (2011) Inertial focusing of non-spherical microparticles. Appl Phys Lett 99(4):044101
34. Iwatsu R, Hyun JM, Kuwahara K (1990) Analyses of three-dimensional flow calculations in a driven cavity. Fluid Dyn Res 6(2):91–102
35. Jeffery GB (1922) The motion of ellipsoidal particles immersed in a viscous fluid. Proc R Soc London A 102:161–179
36. Joseph DD (1990) Fluid dynamics of viscoelastic liquids. Springer, New York
37. Karnis A, Goldsmith HL, Mason SG (1966) The flow of suspensions through tubes: V. Inertial effects. Can J Chem Eng 44(4):181–193
38. Keunings R (2000) A survey of computational rheology. In: Binding DM et al (eds) Proceedings of the 13th international congress on rheology, vol 1. British Society of Rheology, Glasgow, pp 7–14
39. Ku HC, Hirsh RS, Taylor TD (1987) A pseudospectral method for solution of the three-dimensional incompressible Navier-Stokes equations. J Comput Phys 70(2):439–462
40. Lee Y-J, Xu J (2006) New formulations, positivity preserving discretizations and stability analysis for non-Newtonian flow models. Comput Methods Appl Mech Eng 195(9–12):1180–1206
41. Liberzon A, Feldman Y, Gelfgat A (2011) Experimental observation of the steady-oscillatory transition in a cubic lid-driven cavity. Phys Fluids 23:084106

42. Liu YJ, Joseph DD (1993) Sedimentation of particles in polymer solutions. J Fluid Mech 255:565–595
43. Lozinski A, Owens RG (2003) An energy estimate for the Oldroyd-B model: theory and applications. J Non-Newton Fluid Mech 112(2–3):161–176
44. Lynch DR, Gray WG (1979) A wave equation model for finite element tidal computations. Comput Fluids 7(3):207–228
45. McKinley GH (2002) Steady and transient motion of spherical particles in viscoelastic liquids. In: De Kee D, Chhabra RP (eds) Transport processes in bubbles, drops, and particles, 2nd edn. Taylor & Francis, New York, pp 338–375
46. Pan T-W, Chang C-C, Glowinski R (2008) On the motion of a neutrally buoyant ellipsoid in a three-dimensional Poiseuille flow. Comput Methods Appl Mech Eng 197(25–28):2198–2209
47. Pan T-W, Glowinski R (2000) A projection/wave-like equation method for the numerical simulation of incompressible viscous fluid flow modeled by the Navier-Stokes equations. Comput Fluid Dyn J 9(2):28–42
48. Pan T-W, Hao J, Glowinski R (2009) On the simulation of a time-dependent cavity flow of an Oldroyd-B fluid. Int J Numer Meth Fluids 60(7):791–808
49. Pan T-W, Hao J, Glowinski R (2011) Positive definiteness preserving approaches for viscoelastic flow of Oldroyd-B fluids: applications to a lid-driven cavity flow and a particulate flow. In: Ciarlet PG, Glowinski R, Xu J (eds) Handbook of numerical analysis, vol XVI. North-Holland, Amsterdam, pp 433–481
50. Pan T-W, Joseph DD, Glowinski R (2005) Simulating the dynamics of fluid-ellipsoid interactions. Comput Struct. 83(6–7):463–478
51. Patankar NA, Hu HH (2000) A numerical investigation of the detachment of the trailing particle from a chain sedimenting in Newtonian and viscoelastic fluids. J Fluids Eng 122(3):517–521
52. Pironneau O (1989) Finite element methods for fluids. Wiley, Chichester
53. Rallison JM, Hinch EJ (1988) Do we understand the physics in the constitutive equation? J Non-Newton Fluid Mech 29:37–55
54. Segré G, Silberberg A (1961) Radial particle displacements in Poiseuille flow of suspensions. Nature 189:209–210
55. Segré G, Silberberg A (1962) Behaviour of macroscopic rigid spheres in Poiseuille flow Part 1. Determination of local concentration by statistical analysis of particle passages through crossed light beams. J Fluid Mech 14(1):115–135
56. Singh P, Joseph DD, Hesla TI, Glowinski R, Pan T-W (2000) A distributed Lagrange multiplier/fictitious domain method for viscoelastic particulate flows. J Non-Newton Fluid Mech 91(2–3):165–188
57. Süli E (1988) Convergence and nonlinear stability of the Lagrange-Galerkin method for the Navier-Stokes equations. Numer Math 53(4):459–483
58. Süli E (1988) Stability and convergence of the Lagrange-Galerkin method with nonexact integration. In: Whiteman JR (ed) The mathematics of finite elements and applications, VI (Uxbridge, 1987). Academic Press, London, pp 435–442
59. Tagliabue A, Dedè L, Quarteroni A (2014) Isogeometric analysis and error estimates for high order partial differential equations in fluid dynamics. Comput Fluids 102:277–303
60. Wu J (1994) Wave equation models for solving advection-diffusion equation. Int J Numer Methods Eng 37(16):2717–2733
61. Wu J (1997) A wave equation model to solve the multidimensional transport equation. Int J Numer Meth Fluids 24(5):423–439